FLOW CAMBRIDGE
UNIVERSITY PRESS

RESEARCH ARTICLE

Luminescence anisotropy and vorticity magnitude of a free turbulent jet

Markus J. Schmidt[1],* and Thomas Rösgen[1],†

[1]Institute of Fluid Dynamics, ETH Zurich, 8092 Zurich, Switzerland
*Present address: The Fluid Dynamics of Disease Transmission Laboratory, Massachusetts Institute of Technology, Cambridge, Massachusetts 02139, USA. Corresponding author. E-mail: research@schmidt-mail.eu
†roesgen@ethz.ch

Abstract

In the field of experimental fluid dynamics, the direct measurement of vorticity remains a challenge, even though it plays a crucial role in understanding turbulent flows. The present study explores the influence of the rotation of nanoparticles on their luminescence anisotropy as a potential novel measurement method. This relation opens a new field of flow diagnostics, based on the measurement of polarized intensity components. Potentially, the method allows for the direct measurement of the vorticity. For this, the canonical flow in this study is a turbulent round jet at $Re = 12\,000$ and $14\,400$. It is confirmed that the flow regime has an influence on the luminescence anisotropy. Using a model of such deterministic rotations according to another work by the authors (Schmidt & Rösgen, *Phys. Rev. Res.*, vol. 5, no. 3, 2023, 033006), the magnitude of the vorticity components is computed, since the presented set-up is limited to sensing the magnitude of these quantities. The computed components indicate the self-similarity of the vorticity magnitude. A large-eddy simulation is conducted for comparison with the experiments, demonstrating good agreement.

Impact Statement

The vorticity is a crucial parameter in the study of turbulent flow. Until now, the vorticity has been mostly derived from other experimental results, increasing the measurement uncertainty of the results. The present study applies the concept of luminescence depolarization to a free turbulent jet. With the change in anisotropy signals, it becomes possible to compute directly the vorticity magnitudes in the jet. Potentially, the presented novel measurement approach can be further developed for the direct measurement of vorticity. This may facilitate the analysis of flow environments where conventional, gradient-based multiframe methods of vorticity measurement may be difficult to implement. Examples with industrial relevance include high-Reynolds-number boundary layer measurements in turbomachinery and the analysis of highly transient flows such as those near shock waves, but also transport and mixing problems in the small geometries of microfluidics as relevant in biomedical and pharmaceutical applications.

1. Introduction

In the field of fluid mechanics, turbulent flows are one of the most interesting phenomena to observe. Concerning turbulent shear flows, a two-dimensional (2-D) sectional view reveals various features

linked to the fluid rotation. On a large scale, distinct regions with rotational motion can be defined, called eddies. These eddies occur in different sizes, with the largest scales comparable to the outer flow geometry.

The rotational patterns can be described with the concept of local vorticity. The vorticity, defined as the curl of the velocity field, is a primitive variable considered crucial for understanding turbulent flows. The last decades have seen an increased interest in the measurement and computation of vorticity to achieve a more profound understanding of turbulence dynamics. Wallace (2009) provides a retrospective on the insights gained by this research.

To date, various approaches have been developed for the measurement of vorticity. The earliest attempts to measure velocity gradients were based on velocity measurements with hot wires. In this method, an array of several hot wires is designed to measure the microcirculation in a small, finite area. The vorticity is then estimated from the measured circulation (Freytag 1978; Kastrinakis & Eckelmann 1983; Foss, Klewicki & Disimile 1986; Browne, Antonia & Shah 1987; Klewicki & Falco 1990; Vukoslavĉević, Wallace & Balint 1991; Vukoslavĉević & Wallace 1996; Zimmerman, Morrill-Winter & Klewicki 2017; Zimmerman *et al.* 2019). While thermal anemometry measurements have a high temporal resolution, it remains challenging to resolve the spatial dimensions. Several parameters have to be considered. The Kolmogorov scale of the turbulent flow defines the desired resolution regarding diagnostics. In contrast, the probe's mechanical design and the influence of several wires on the downstream flow contradict this goal. The problem is discussed in detail by Wallace & Foss (1995).

The measurement of velocity components and the computation of their gradient with non-intrusive optical methods have also been employed. The capabilities of laser Doppler anemometry, the measurement of a velocity component using the frequency shift due to the Doppler effect, have been extended to multiprobe measurements for the indirect measurement of vorticity (Lang & Dimotakis 1984, 1986; Agui and Andreopoulos 2003).

The methods involving the observation of particles in fluid flows, particle image velocimetry (PIV) and particle tracking velocimetry (PTV), have gained attention and popularity in the last decades. Both methods are capable of computing the velocities from the measured displacements of particles seeded into the flow. The gradients can be computed from these velocity fields, providing information about vortical structures (Lourenco & Krothapalli 1986; Meinhart & Adrian 1995; Hu *et al.* 2001; Kähler 2004; Ganapathisubramani *et al.* 2005). Recently, the use of tomographic techniques with PTV allowed computing all vorticity vector components. Schneiders, Scarano & Elsinga (2017) measured a turbulent boundary layer with a tomographic PTV set-up and computed the vorticity field.

The spatial resolution remains a challenge in measurements with optical anemometry. In high-resolution dual-plane PIV measurements, the spatial scales depend on the light sheet thickness and separation, the PIV correlation window size, the bad vector replacement region size and the smoothing filter scale. Buch & Dahm were able to resolve the small-scale structure of scalar mixing within the Kolmogorov length scale (Buch & Dahm 1996, 1998).

One of the first studies to directly measure vorticity were Frish & Webb (1981). They incorporated reflective surfaces in spherical transparent beads. These 20-micrometre particles were seeded into a flow and illuminated with a laser sheet. By tracking the reflection position change, they could compute the reflection angle and hence the beads' rotation. Wu, Xu & Bodenschatz (2019) measured the vorticity in a Taylor–Couette flow with hydrogel particles. They incorporated small mirrors in micrometre-sized hydrogel particles and used them as tracers.

Recently, Ryabtsev *et al.* (2015, 2016) measured the vorticity in the centre of a rotating cylinder by utilizing the rotational Doppler effect. Laser light with a defined orbital angular momentum was focused on the centre of the rotating cylinder. The intensity modulation was measured with a photodiode from the interference pattern with a reference beam, and the vorticity was subsequently computed.

The present study examines the potential of luminescence anisotropy for the measurement of fluid rotation. The optically anisotropic behaviour has been utilized in flow diagnostics before. Kenyon *et al.* attempted to study the molecular alignment of dye molecules in flows (Kenyon, McCaffery & Quintella

1991*a*; Kenyon *et al.* 1991*b*). A solution of Rhodamine 6G in ethylene glycol passed a microscale slit of 500 micrometres and entered the ambient air. The resulting jet was excited with a polarized laser beam, and the fluorescence anisotropy signal was acquired in the direction of the laser beam. The polarization was analysed with a photoelastic modulator and a lock-in amplifier. They noted a change of polarization within the region of a free jet at $Re = 600$ and 1100.

Furthermore, a jet with the dyes rhodamine 6G and resorufin in ethylene glycol was studied to resolve polarized fluorescence in the picosecond range (Bain, Chandna & Bryant 2000*a*; Bain *et al.* 2000*b*). The molecular alignment in the medium, as well as the depolarization at different positions in the jet, were temporally resolved.

He & Lu (2020) used acquisitions with a polarization-sensitive camera to visualize the interaction between a shock wave and a boundary layer.

Recently, Park, Shakya & King (2019) studied the depletion layer dynamics of complex fluids in a laminar Poiseuille flow. By examining a polyelectrolyte solution with dye molecules, they could deplete the complex molecules near the walls due to different depolarization. The depolarization depends on the amount of the monomer polyelectrolyte poly (styrene sulfonate) because the dye's rotation can be influenced if it is in proximity to this monomer.

Despite continued research in the field of vorticity measurement, adequately measuring this fundamental property remains a significant challenge. The various methods have their advantages and disadvantages and may be evaluated on their cost, complexity and performance while providing an adequate spatial and temporal resolution. This article examines experimentally the utilization of luminescence anisotropy for the measurement of fluid–particle rotation. The technique is based on the model for deterministic rotations in the luminescence anisotropy as outlined by the authors in Schmidt & Rösgen (2023).

The basic concept relies on the idea of flow-induced depolarization of an initially polarized excited population of dye molecules.

The goal of the present work is to examine the potential and limitation of luminescence anisotropy as a physical principle for the direct measurement of vorticity in turbulent flows. A free round jet at $Re = 12\,000$ and $14\,000$ is examined experimentally. With a model for the observable optical response, the vorticity magnitude is computed. This magnitude is compared with results from a large-eddy simulation (LES) study. The goal is to evaluate the applicability of luminescence anisotropy as a method for the measurement of vorticity.

2. Experimental requirements and limitations

In experimental fluid mechanics, existing and novel methods for measuring vorticity have to meet several requirements. Regarding turbulent phenomena, spatial and temporal resolution is of great importance. In this context, the scaling concepts introduced by Kolmogorov are widely adapted. The smallest length and time scales are defined spatially by the viscous scale $\eta_d = \nu^{3/4}\epsilon^{-1/4}$ and $T_\epsilon = \nu^{1/2}\epsilon^{-1/2}$ with ϵ as the turbulent dissipation rate and ν the kinematic viscosity. A suitable method should ideally be capable of resolving these smallest scales in turbulent flows. In addition, it should be capable of resolving all components simultaneously to account for the dynamic nature of turbulence. In the following, various existing methods are presented which partially fulfil these requirements in different respects.

Polarization anisotropy measurements are rarely applied in experimental fluid dynamics. One notable application is dual-plane PIV, in which two planes with different polarization are established (Hu *et al.* 2001; Kähler 2004; Ganapathisubramani *et al.* 2005). With two cameras, each recording one of the polarized planes, it is possible to resolve the velocity gradients and compute the vorticity. The method uses polarization only qualitatively to distinguish the two laser sheets, but does not require intensity-sensitive postprocessing. Thus, a comparable method should exceed the spatial resolution of PIV measurements while resulting in a significantly lower measurement error.

In other fields of science, anisotropy measurements are often averaged and do not provide spatial information. A frequent use of spatial anisotropy information is in the field of fluorescence anisotropy imaging (Siegel *et al.* 2003; Ströhl *et al.* 2018). The method was established in biology and is usually applied in a set-up with a microscope. The anisotropy of a sample is analysed considering its fluorescence anisotropy. In contrast to conventional experiments in fluid dynamics, the optics and calibration procedures involved differ significantly. Due to spatial limitations, the emission is acquired on the same path as the excitation, necessitating additional separation optics. The following sections describe the experimental procedures for anisotropy measurements in the specific context of experimental fluid dynamics. These considerations pertain to the set-up, calibration procedure and selection of a suitable tracer.

2.1. Requirements for polarization measurements

High-precision polarization measurements are not common in experimental fluid dynamics. A crucial requirement is the measurement of highly polarized signals with low error and the establishment of a high polarizing efficiency.

This translates into the following specifications.

(i) For 2-D measurements with three components of the average absolute vorticity, a pulsed excitation with a laser sheet is sufficient. Theoretically, an existing PIV set-up can be used.
(ii) This set-up has to be equipped with linear polarizers and waveplates to manipulate the laser beam's polarization and to acquire polarized signals with the camera.
(iii) For the laser, two different polarization orientations are necessary. The camera has to acquire two distinct polarizations.
(iv) The acquired signals have to be corrected for the spatial variations in polarizer efficiencies. This correction is realized with the so-called G-factor.

2.2. Particles

The Brownian correlation time is of the order of nanoseconds for molecules, which is too fast for most of the known flow regimes to acquire a good signal. The rotation information is lost due to the immediate decorrelation by this stochastic process. Furthermore, the assumption of continuum mechanics does not hold on a molecular scale. It follows that spherical particles with a diameter large enough to eliminate Brownian motion are required for measurements of fluid rotation. Theoretically, the particles might be of a size to detect them individually, as in PIV or PTV. A problem would arise for the correct computation of intensity since such a particle would cover several pixels, most of them only partially. This analysis would require complicated processing of the effective intensity signal from each particle. As a consequence, nanoparticles are used so as to avoid such postprocessing problems. Another advantage is the minimization of single-particle errors, since a larger population is acquired per pixel of the camera.

Only a few dyes and suppliers are available for phosphorescent particles with suitably long lifetimes. Some commonly used particles in PIV and PTV which were stained with xanthene dyes were examined by Schmidt & Rösgen (2021*c*), but the short luminescent lifetime ultimately renders them unsuitable for most low-speed flows.

As an alternative, polystyrene (PS) particles with the lanthanide europium in its oxidation state +3, incorporated in the polymer matrix, are commonly used and commercially available. The group of lanthanides exhibits slow emission rates, resulting in longer lifetimes (Richardson 1982; Mushrush *et al.* 1986; Balzani & Ballardini 1990; Sabbatini, Guardigli & Lehn 1993; Li & Selvin 1995). Since the absorption of the lanthanides is weak, they are excited in the form of metal–ligand complexes (Lakowicz 2006*b*, pp. 87–88). The delayed fluorescence of these complexes has previously been applied for time-gated detection in immunoassays by Hemmilä (1993). A novel development by Spherotech, the Sphero EUP-025-5 europium PS particles, incorporates such an Eu(III)–ligand complex and is used in

this work. The mean diameter is 380 nm according to the supplier. The standard deviation in diameter should not influence measurement results, since the signal of a larger population is averaged per pixel.

2.3. Particles and microscales

An important consideration is the method's sensitivity, as detailed by Schmidt & Rösgen (2023). The sensitivity depends on the expected vorticity ω, the luminescence lifetime τ_l and the Brownian correlation time τ_{br}. The volume flow rate and thus the expected vorticity magnitude should ideally be adjusted to match with the sensitivity constraint $\omega\tau_l \approx 1$. Additionally, the relation between the luminescence lifetime τ_l and the Brownian correlation time τ_{br} is essential. The particles with an average diameter of 380 nm have a Brownian correlation time of 6.1 ms in water at room temperature. The luminescent lifetime of the particles has been experimentally determined to be (248.2 ± 1.7) µs (Schmidt 2021). Thus, the Brownian correlation time is 25 times longer than the luminescence lifetime. Consequently, the decorrelation due to Brownian motion should only have a minor influence on the anisotropy.

A further factor is the particles' response time to the flow. The translational relaxation time can be estimated with $\tau_u = 2R_{tr}^2\rho_{tr}/(9\mu)$, while the rotational relaxation time is $\tau_r = 2R_{tr}^2\rho_{tr}/(15\mu)$, with R_{tr} as the radius of the tracer particle, ρ_{tr} the density of the tracer particle and μ the dynamic viscosity of the fluid (Brenner 1964). For the used PS particles in water at room temperature, the relaxation times become $\tau_u = 9.5$ ns and $\tau_r = 5.7$ ns with $\rho_{tr} = 1.18$ g cm^{-3} and $\mu = 0.001$ Pa s. Thus, the time scales are significantly shorter than any turbulence time scale by several orders of magnitude.

The spatial resolution depends solely on the resolution of the optical system. In the present set-up, one pixel represents 89 µm at the imaging plane. This resolution can be compared to the Kolmogorov microscale λ_K. Dimotakis estimated the scale for a free round jet with $\lambda_K = 0.95\delta_r(z)Re^{-3/4}$, with $\delta_r(z) = 0.4(z - z_0)$ the dimensional jet width at streamwise position z (Dimotakis 2000, (22)). Hussein *et al.* estimated the virtual origin of a free jet with $z_0 = 4d$ (Hussein, Capp & George 1994, figure 4). Thus, the smallest expected Kolmogorov length scale at $z = 50d$ and $Re = 14\,400$ is 5.4 µm, which results in a ratio to the spatial resolution of 0.06. Note that the spatial resolution could be increased with a focus on the self-similar region.

In contrast to methods with direct particle imaging such as PIV and PTV, individual particles are not resolved by the implemented optical system. With the assumption of a laser sheet thickness of 1 mm, approximately 4100 particles are captured per pixel at the chosen concentration.

2.4. Set-up

The general set-up can be found in figure 1. The light source is a Continuum Surelite PIV laser with a custom optical set-up, operating at the third harmonic of 355 nm. The third harmonic is generated with a Continuum THG-PL9K. This third-harmonic generator is designed for a dual output of the second harmonic at 532 nm and the third at 355 nm. Hence, two Thorlabs HBSY134 harmonic beamsplitters are inserted into the beam path, one inside the laser casing and the second outside, reflecting the third harmonic and collecting the second harmonic in the beam dumps (not shown in figure 1).

For attenuation of the beam, an Eksma 460-4240 Nd:YAG zero-order $\lambda/2$ waveplate (WP1) is used. With a change in polarization orientation, it is possible to attenuate the laser beam with the beam polarizer (PL). The polarization of the beam is then controlled with a Thorlabs GLB10 Glan Laser alpha-BBO Polarizer (PL). For the anisotropy measurements, two different orientations are required for the excitation source. Hence, a Thorlabs WPH05M-355 zero-order $\lambda/2$ waveplate (WP2) is used to change the laser polarization from vertical to horizontal. Next, an iLA LSO mini light sheet optic is used to shape the beam into a light sheet. The design wavelength of the sheet optic is at 532 nm, and attenuation leads to ≈ 0.4 of the laser's maximal power at the experiments' 355 nm wavelength. The attenuation is chosen to minimize the effect of photobleaching of the dye for measurements with many excitations.
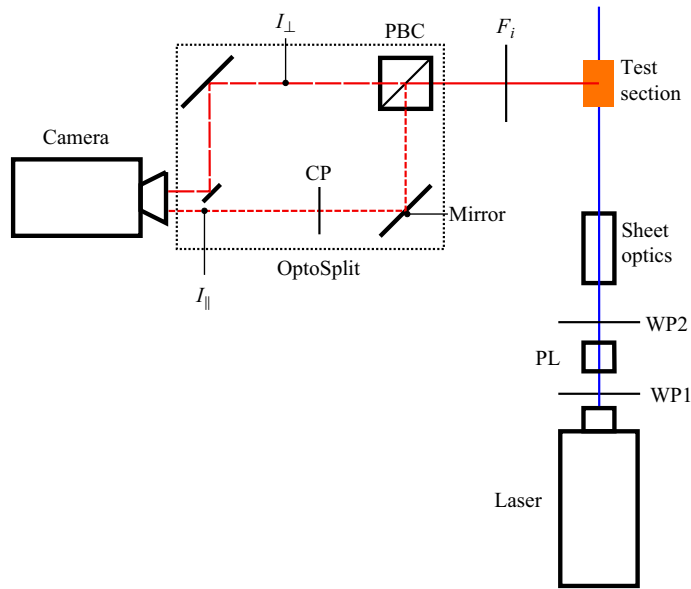
Figure 1. *Experimental set-up for anisotropy measurements. The laser light polarization is defined by the polarizer (PL). The pulse energy can be attenuated with the first $\lambda/2$ waveplate (WP1). A second waveplate (WP2) can be inserted and alters the polarization direction by 90°. A laser sheet optic is used to create a light sheet in the test section. The camera is equipped with a series of filters (F_i) to attenuate scattered laser light and other fluorescence from unwanted sources. The OptoSplit is operated with a linear polarizing beamsplitter cube (PBC), dividing the signal into perpendicular and parallel signals ($I_\parallel$, $I_\perp$). These signals are projected onto separate regions of the camera chip. The reflected beam ($I_\parallel$) yields only a low degree of polarization. Thus, a cleanup polarizer (CP) is added.*

On the emission side, a PCO Sensicam QE, a Nikon AF Micro Nikkor 105 mm objective, a Schott KV550 longpass filter and a Salvo Technologies 2021OFS-643 643 nm edge filter are used (F_i). Between the camera and the objective, a Cairn Research OptoSplit II ByPass is mounted. This device separates the signal into its polarization components and projects them onto different areas of the camera sensor. The OptoSplit is equipped with a Thorlabs PBS251 polarizing beamsplitter cube (PBC). Since the reflected beam only provides a poorly polarized signal with a contrast of 1 : 20 to 1 : 100, an additional cleanup polarizer (CP) is inserted into the reflected beam path.

The arrangement of the test section can be found in figure 2. The coordinate system is defined with x as the observation direction, y the direction of laser beam propagation and z the jet propagation direction. A glass capillary with a diameter of 0.4 mm is used as a round channel to establish the flow. The length of the capillary is 100 diameters. The fluid exits the capillary into a cuboid. The cuboid's height in the streamwise direction is 310 diameters, while the quadratic side length is 110 diameters. This width is chosen to reduce recirculation within the measurement volume. On the side opposite to the capillary, the fluid leaves through a 5 mm nozzle. Thus, the flow should not form a stagnation region in the cuboid.

The laser sheet's entrance side features a quartz glass insert to avoid laser light interaction and attenuation. The jet is oriented with its streamwise direction pointing downward, aligning the flow with gravity. The laser sheet is focused on the centreline of the jet. The sheet has an approximate thickness of 1 mm at its focal waist. Hence, a 2-D acquisition assumption can be considered valid at downstream positions where the jet has grown significantly larger than the laser sheet thickness. Since the alignment is done visually without a calibration target, the procedure may introduce a small error for measurements directly at the capillary exit.
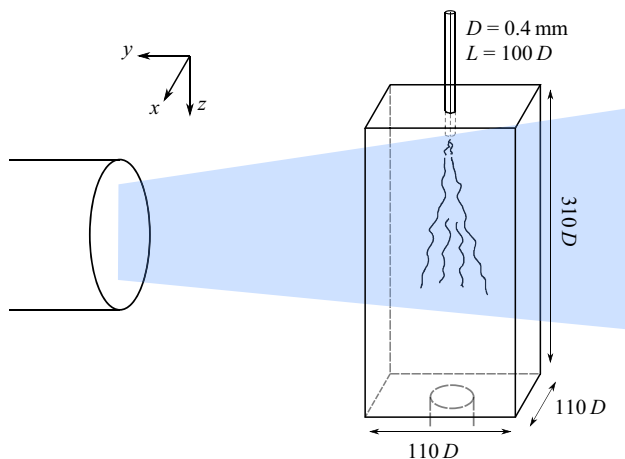
Figure 2. *Orientation of the jet experiment. The laser is expanded into a light sheet. It is adjusted to pass through the centreline of the jet. The observation is in the x direction. Acquisition with two different polarization orientations is required. These orientations are in the x and z directions. The orientation is chosen due to experimental and space constraints.*

The flow is established using a Cetoni neMESYS 2600N high-pressure syringe pump. The pump is equipped with a stainless-steel high-pressure syringe with a nominal volume of 50 ml. The pump is connected to a Cetoni neMESYS 3/2-way ball valve. The valve enables the aspiration from the reservoir and dispersion into the flow cell in an automated fashion. A sample of 0.5 L with Spherotech Sphero EUP-025-5 europium polystyrene particles in a deionized water suspension with a concentration of 0.015 mg mL^{-1} is used in the experiments.

2.5. The G-factor correction

On the emission side, the polarizers' efficiencies have to be considered for the correct computation of the anisotropy. The G-factor represents these. In the literature, classical approaches for anisotropy measurements are the L and the T-format (Lakowicz 2006a, pp. 361–364). The letters symbolize the beam path. For example, the L-format is defined by the excitation and observation being at a right angle and the test section in the letter's corner, forming an L. The emission polarizer has to be rotated to acquire the different polarization signals. In contrast, the T-format observes the sample from opposite sides, forming a T and enabling a simultaneous measurement. In the present work, the measurement can be regarded as a mixture of the two, observing in L-format but acquiring both components simultaneously as in the T-format.

While measurements are aligned as in the L-format, two separate polarizers are used in the set-up. A schematic overview can be found in figure 3. Each polarization channel has an efficiency S_i. The respective intensities depending on the polarization orientation of the excitation laser light are given by

$$\frac{I_{HV}}{I_{HH}} = \frac{S_\parallel I_\perp}{S_\perp I_\perp} = G \qquad \text{and} \tag{2.1}$$

$$\frac{I_{VV}}{I_{VH}}\frac{1}{G} = \frac{I_{VV}I_{HH}}{I_{VH}I_{HV}} = \frac{I_\parallel}{I_\perp}, \tag{2.2}$$

with S_i the polarization efficiency in i, G the G-factor and I_{ij} the experimental intensity signal with excitation in i and emission in j.
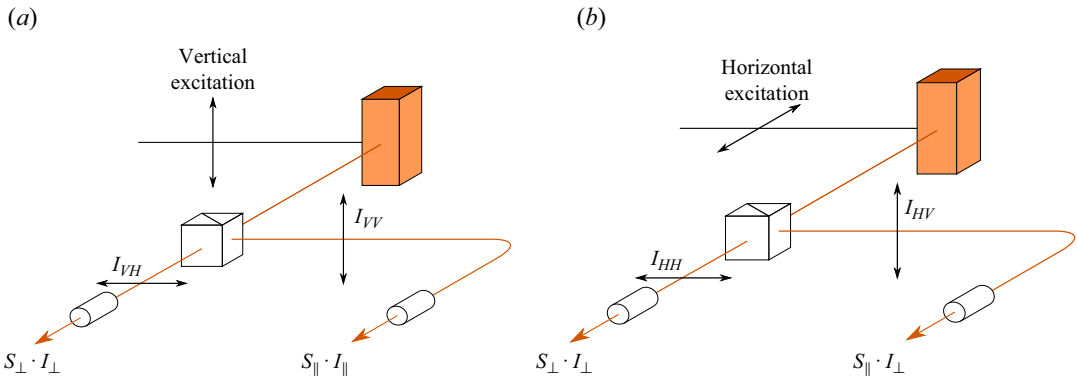
(a)

(b)

Figure 3. *Principal polarizer alignment for G-factor computation with vertical (a) and horizontal (b) excitation orientation. Each polarization channel has a unique efficiency. With a horizontal polarization, the intensities $I_\perp$ without the influence of the polarizers are theoretically equal.*

As with the T-format, there are two possibilities to correct the anisotropy for the efficiencies:

$$r = \frac{I_\parallel/I_\perp - 1}{I_\parallel/I_\perp + 2} \tag{2.3}$$

$$= \frac{I_{VV} - GI_{VH}}{I_{VV} + 2GI_{VH}}. \tag{2.4}$$

The advantage of the G-factor used in (2.4) is its independence of the degree of anisotropy. This can be used for the correction and computation of intensity relations only by correction of the horizontal component, in contrast to the relative correction in (2.3).

Furthermore, the camera's efficiency and behaviour have to be considered, necessitating the use of a spatially resolved G-factor. In this work, the correction with G-factor is used implicitly and without further discussion in the upcoming sections, applying it to the horizontally polarized images.

3. Experiments

Two Reynolds numbers ($Re = 12\,000$ and $14\,400$) are investigated. In these experiments, the flow conditions at rest are measured first to ensure a proper G-factor correction and fundamental anisotropy computation. Two different excitation polarization orientations are used for image acquisition. Referring to the G-factor correction, the laser polarization is set perpendicular (excitation in z) and parallel (excitation in x) with respect to the axis of observation x. In total, there are four independent measurements with two emission polarization orientations each per Reynolds number. A sample of 500 images is taken per experiment. For each image, the exposure time is set to 8 s, effectively accumulating 80 luminescent decays bases on 10 laser pulses per second. The total number of images per syringe stroke depends on the volume flow. For $Re = 12\,000$ and $Re = 14\,400$, two images and one image are acquired per stroke, respectively. The Reynolds numbers correspond to the jet velocities U_j at the nozzle of 26.6 m s^{-1} and 32.0 m s^{-1}, respectively. The results with excitation in x without flow are used for G-factor computation. The data is readily available in a repository (Schmidt & Rösgen 2021*a*).

4. Results

4.1. Anisotropy change due to flow

For the computation of anisotropy, the images are background-subtracted and averaged. The component in x is then G-factor corrected prior to anisotropy computation. Figures 4–6 show the results for no-flow,
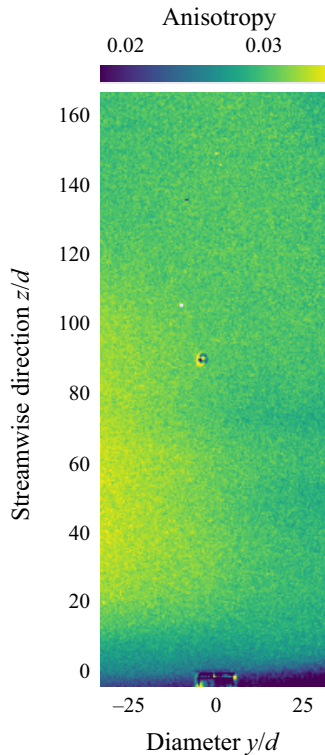
Figure 4. *Anisotropy without flow for excitation polarization in z. The artefact at z/d = 90 is an air bubble at a glass window.*

$Re = 12\,000$ and $Re = 14\,400$, respectively. A change in the anisotropy for excitation in z is observable. The shape of the jet can be identified through the anisotropy change. In contrast, the anisotropy with excitation in x does not change due to the flow. This behaviour is predicted in the model by the authors (Schmidt & Rösgen 2023). The figures show spherical artefacts at various positions. These artefacts are air bubbles at the glass window. In figure 4, the anisotropy field shows spatial inhomogeneities. These inhomogeneities are due to depolarization effects of the laser sheet and do change with different focus settings of the laser sheet optics. The mean vorticity has the dominant component out-of-plane in x. With the polarization orientation of the excitation laser being in x as well, the anisotropy changes are insensitive to changes in this direction. This alignment is supposed to be sensitive to the ω_y and ω_z components, which do nearly vanish in the jet's centre plane. Of interest are the three distinct regions of the jet. For the result of $Re = 12\,000$, there is a cylindrical flow region with the diameter of the nozzle until approximately 20 diameters. The transition region follows this phenomenon up to 60 to 70 diameters. After approximately 70 diameters, the jet enters the region of self-similarity.

The standard error is computed for the anisotropy maps for each individual pixel across the 500 acquired images. The standard errors for the anisotropy at $Re = 12\,000$ are evenly distributed. The mean standard error is 0.0028 and 0.0026 for polarization orientation in x and z, respectively. Thus, the relative error of the anisotropy in figure 5 (polarization in z; figure 5b) is around 10 % in the slow flow regions and up to 15 % at the centre of the jet. The errors for $Re = 14\,400$ are not presented here, but are of similar magnitude.

4.2. *Computation of absolute vorticity*

In a next step, the measurement data is taken to compute the average absolute vorticity. The underlying theory is described in detail by Schmidt & Rösgen (2023). In our previous work, the problem was not
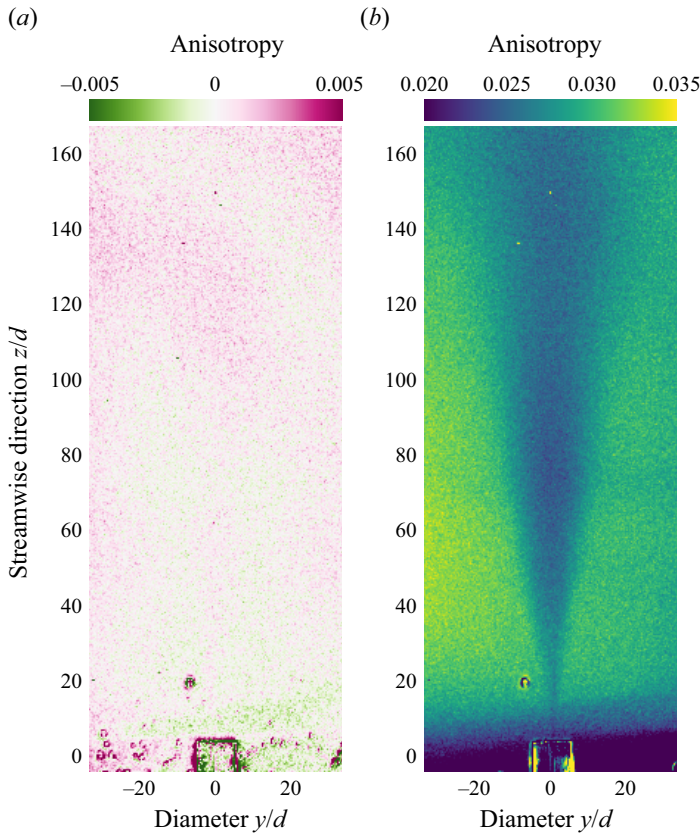
(a)   (b)

Anisotropy   Anisotropy

Figure 5. *Anisotropy at Re* = 12 000 *for excitation polarization in x (a) and z (b). The artefact at z/d = 20 is an air bubble at the glass window.*

solved analytically. Thus, an optimization with an objective function is defined to find a solution. The objective function is designed to only use signals from the same measurement. The photobleaching of the particles would introduce an error in objective functions with cross-computation of the experimental results. Thus, an objective function consisting of two fractions is defined in a way that only intensities from the same experiments are compared,

$$o = \left(\frac{D_{zz,exp}}{D_{zy,exp}} - \frac{D_{zz,a}}{D_{zy,a}} \right)^2 + \left(\frac{D_{xz,exp}}{D_{xy,exp}} - \frac{D_{xz,a}}{D_{xy,a}} \right)^2, \quad (4.1)$$

with $D_{....}$ the integrated intensity signal for a single shot excitation, the first subscript indicating the polarization orientation of the excitation laser (x or z), the second subscript the acquired polarization component with the camera (y or z) and the third subscript defining if the signal is from the experiments or the analytical solution (a or exp). The analytical solutions for the cases are discussed and derived by the authors (Schmidt & Rösgen 2023, (28)–(33)) and are used to find the solution of the vorticity components.

It has to be noticed that the objective function only includes the signals from the flow measurements. However, the no-flow images are used to compute the G-factor to correct the anisotropy computation. The objective function is utilized in the Python toolbox pyoptivorticity (Schmidt & Rösgen 2021b), based on the theory by Schmidt & Rösgen (2023). The measured anisotropy without flow is used to
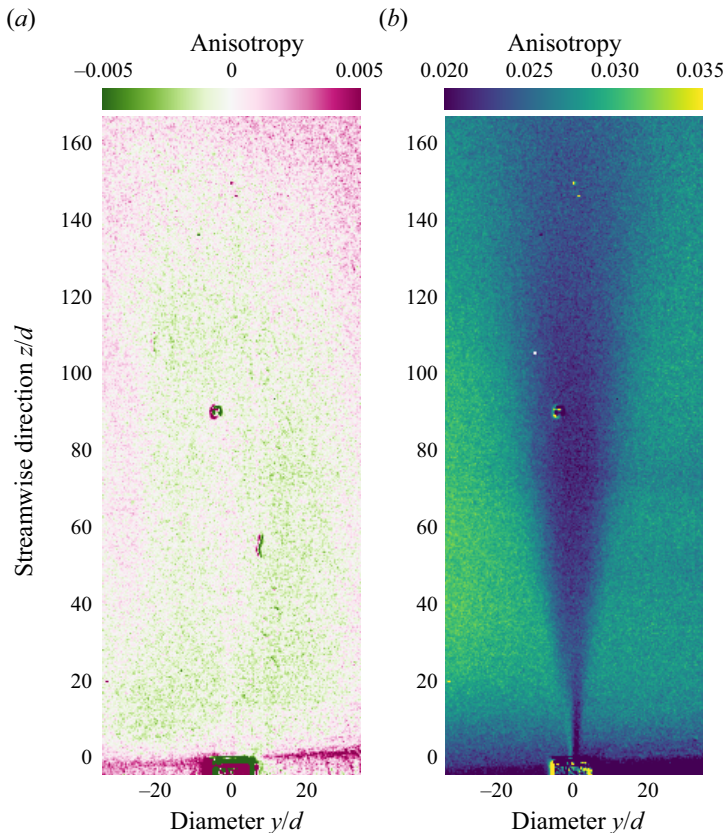
Figure 6. *Anisotropy at Re = 14 400 for excitation polarization in x (a) and z (b). The artefact at z/d = 90 is an air bubble at the glass window.*

compute the fundamental anisotropy r_0 with the Perrin equation

$$r_0 = r_m \left(1 + \frac{\tau_l}{\tau_{br}} \right), \tag{4.2}$$

with r_m the measured anisotropy.

Figures 7 and 8 show the results for $Re = 12\,000$ and $14\,400$, respectively. The vorticity magnitude is normalized with the jet diameter d and jet exit velocity U_j. It resolves the dominant component of vorticity correctly in x. The used optimization package pyoptivorticity is available in a repository (Schmidt & Rösgen 2021b).

5. Comparison in self-similar region of the jet

The measurement of vorticity in this specific experiment has two limitations. These have to be taken into account for a comparison with model results in the self-similar regime. First, the two distinct emission polarization components available can resolve the absolute vorticity, but not its sign. Second, due to the dye's low quantum yield, the full luminescence decay must be acquired for a sufficient intensity signal. The signal should exceed the noise level of the camera to be able to compute the vorticity components. With the current flow velocities, the particle may travel several diameters during the luminescence lifetime τ_l. With the given experimental parameters, the jet exit velocity can result in the advection of the tracers up to $10d$ within the lifetime τ_l. Thus, a simple comparison with the self-similar solutions
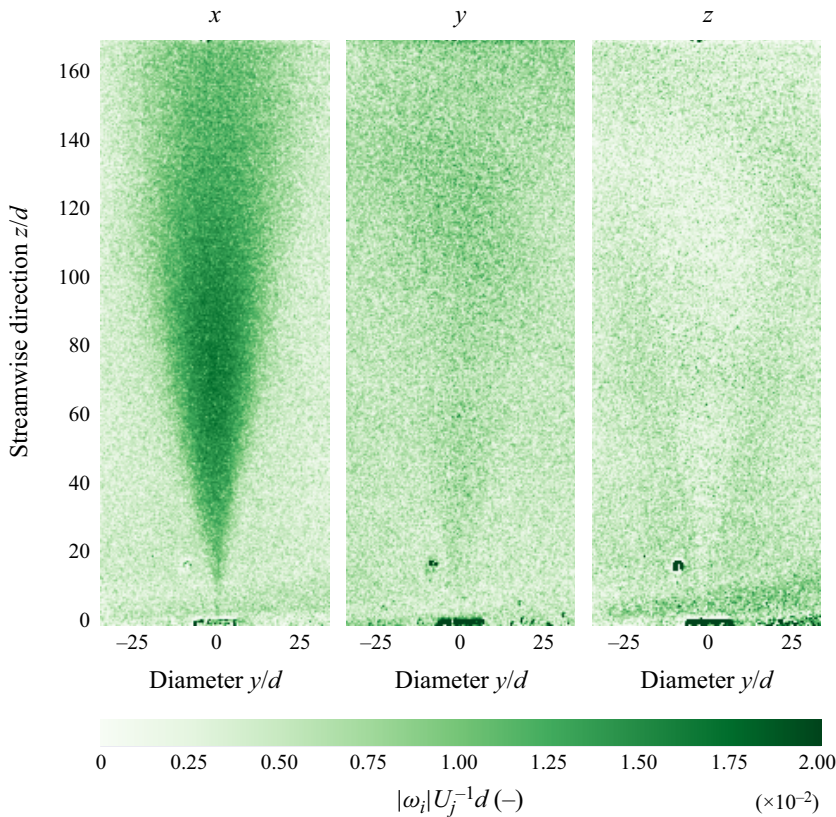
Figure 7. *Optimization results for the normalized absolute vorticity $|\omega_i|U_j^{-1}d$ at Re = 12 000. The normalized vorticity components are x to z from left to right.*

of vorticity is not warranted. For comparison, a time-resolved simulation of the vorticity is required to compute the average absolute vorticity field.

5.1. Large-eddy simulation

With the presented set-up, only the absolute of the vorticity can be measured, but the available research data does not provide comparisons for this flow property. Thus, a LES is performed to compare with the experimental findings. A three-dimensional domain is computed with the Smagorinsky subscale turbulence model. The method has been successfully applied before and proven appropriate for shear flows in jets (Olsson & Fuchs 1996; Gohil, Saha & Muralidhar 2014). The simulation is set up with COMSOL 5.6. The computational domain has a conical shape with a streamwise length of $65d$, a diameter of $3d$ at the inflow, and a larger diameter of $19.5d$ in the far field, resulting in an irregular tetrahedral grid with approximately 1 600 000 elements. The flow is computed at a Reynolds number of 12 000. The simulation is computed up to the non-dimensional time of $\bar{t} = tU_jD^{-1} = 7664$ to achieve stationary conditions. The simulation is continued up to $\bar{t} = 14\,328$, and the results are averaged azimuthally.

5.2. Self-similarity of the absolute vorticity

For the streamwise velocities, the profiles are normalized to the jet width δ and the centreline velocity to achieve self-similarity. In the analysis, the vorticity $|\omega_x|$ is normalized similarly, with the corresponding
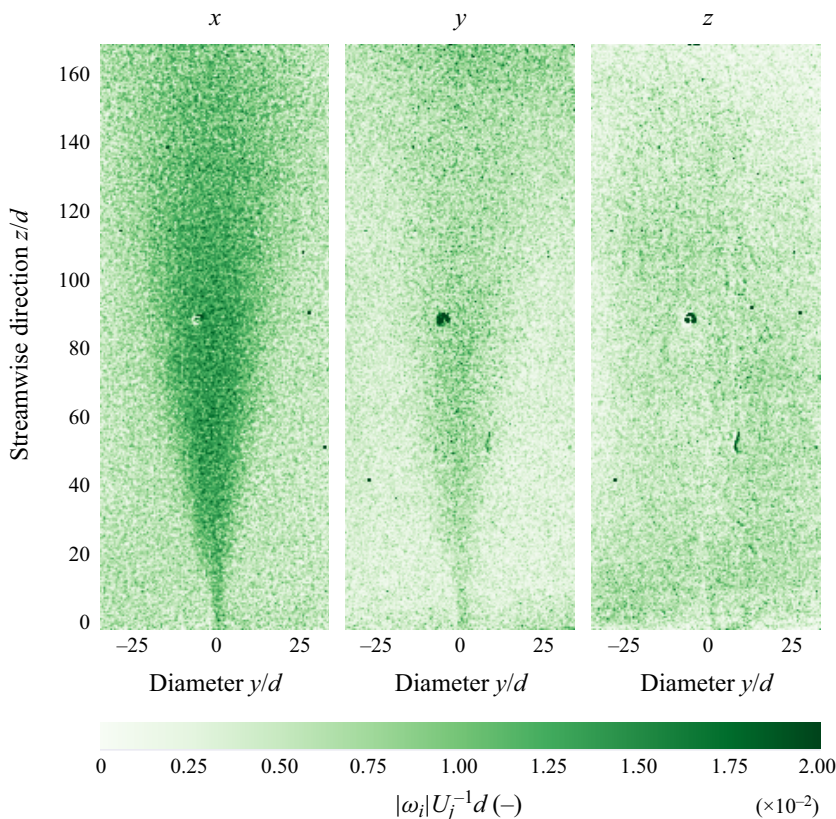
Figure 8. *Optimization results for the normalized absolute vorticity $|\omega_i|U_j^{-1}d$ at Re = 14 400. The normalized vorticity components are x to z from left to right.*

centreline vorticity $|\omega_{x,c}|$. For the results of $|\omega_x|$ in figure 7 (at $Re = 12\,000$) the normalized spreading rate is determined to be 3.3. The results for several cross-sections are shown in figure 9. A Gaussian filter with a standard deviation of three pixels of the kernel has been applied to the data. It can be seen that the absolute value of the vorticity exhibits self-similarity, with a profile resembling that of a jet velocity distribution.

The results from the LES are averaged azimuthally, resulting in a half-plane of vorticity magnitude The computed values are also shown in figure 9, and are in good agreement with the experimental findings. The integration of the intensity signal due to advection of particles was not considered for this comparison of experimental and numerical results.

6. Conclusion

The experiments examined the possible use of luminescence anisotropy for the direct measurement of flow vorticity.

A turbulent round jet was examined at $Re = 12\,000$ and $14\,400$. A theory for the influence of a deterministic rotation on the anisotropy was applied. The model describes the observability of vorticity component magnitudes following the acquisition of the complete luminescence decay after pulsed excitation (Schmidt & Rösgen 2023). A change in anisotropy was predicted, and a corresponding average absolute vorticity component was computed with an optimization toolbox based on this model. A LES was computed for comparison with the experimental findings. The simulation is in good agreement with
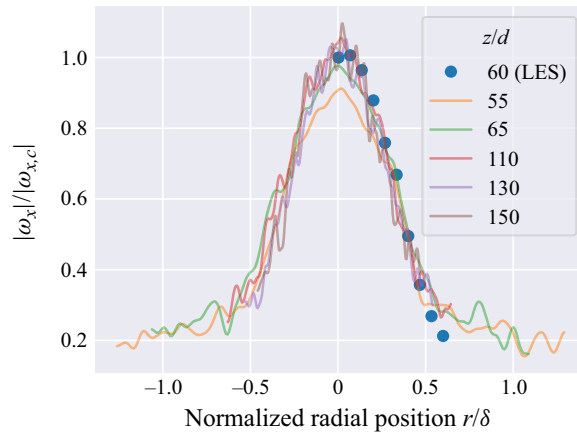
Figure 9. *Normalized average absolute vorticity at different streamwise positions. A Gaussian filter ($\sigma = 3$) is applied to the experimental results (lines). Results of the azimuthally averaged of the LES are provided as well (blue dots).*

the experimental data. It was shown that the vorticity magnitude exhibits self-similarity similar to the velocity.

The current experimental set-up is capable of measuring four distinct polarized signals. Changes in luminescence anisotropy, computed from the signals, compared with no-flow conditions can be observed. Furthermore, the absolute vorticity can be computed from these signals. The sensitivity is highest in the range of $\omega\tau_l = 1$, as shown by Schmidt & Rösgen (2023). This relation holds under the assumption of a negligible, e.g. sufficiently large, Brownian correlation time and acquisition of the complete luminescence decay. It has to be pointed out that the sensitivity depends on the shortest relevant time constant. On the one hand, the Brownian correlation time can be shorter than the luminescence lifetime, $\tau_{Br} \ll \tau_l$. On the other hand, reducing the exposure time below the luminescence lifetime will lead to a sensitivity depending on this exposure time instead (Schmidt & Rösgen 2023). A reduction of exposure time is imperative for the application of the method in a turbulent flow. A limitation of the experiments so far remains the long exposure time compared with the flow's time scales, which leads to spatial integration of the signals.

For time resolved measurements, the quantum yield of the particles in combination with the camera is not sufficient for single shot measurements. On the instrumentation side, a gated, intensified camera might achieve a higher sensitivity. On the downside, the intensifier of such a camera has a significantly higher noise level than the cooled charge-coupled device used in this article, especially for the computation of anisotropy maps. Thus, the application of an intensified camera requires more experimental testing for a thorough assessment. It appears feasible to reduce the acquisition time with a gated camera for faster flow regimes, effectively coupling the sensitivity range to this exposure time. For the reduction of the exposure time, further research on suitable phosphorescent tracers is required.

The indifference to the sign of the vorticity may in principle be overcome with a different arrangement of polarizers. The theory for directional vorticity measurements would have to be developed further, following the approach outlined in Schmidt & Rösgen (2023). The latest polarization cameras enable the simultaneous acquisition of four polarization directions. Conceptually, such a camera should be able to resolve the signed *x*-component of the vorticity, for example, again in a turbulent round jet experiment.

Declaration of interests. The authors declare no conflict of interest.

Author contributions. M.J.S. and T.R. created the research plan, designed experiments, and formulated the analytical problem. M.J.S performed all experiments and postprocessing. M.J.S. and T.R. wrote the manuscript.

References

AGUI, J.H. & ANDREOPOULOS, Y. 2003 A new laser vorticity probe – LAVOR: its development and validation in a turbulent boundary layer. *Exp. Fluids* **34** (2), 192–205.

BAIN, A.J., CHANDNA, P. & BRYANT, J. 2000*a* Picosecond polarized fluorescence studies of anisotropic fluid media. I. Theory. *J. Chem. Phys.* **112** (23), 10418–10434.

BAIN, A.J., CHANDNA, P., BUTCHER, G. & BRYANT, J. 2000*b* Picosecond polarized fluorescence studies of anisotropic fluid media. II. Experimental studies of molecular order and motion in jet aligned rhodamine 6G and resorufin solutions. *J. Chem. Phys.* **112** (23), 10435–10449.

BALZANI, V. & BALLARDINI, R. 1990 New trends in the design of luminescent metal complexes*. *Photochem. Photobiol.* **52** (2), 409–416.

BRENNER, H. 1964 The Stokes resistance of an arbitrary particle–III: shear fields. *Chem. Engng Sci.* **19** (9), 631–651.

BROWNE, L.W.B., ANTONIA, R.A. & SHAH, D.A. 1987 Turbulent energy dissipation in a wake. *J. Fluid Mech.* **179**, 307–326.

BUCH, K.A. & DAHM, W.J.A. 1996 Experimental study of the fine-scale structure of conserved scalar mixing in turbulent shear flows. Part 1. $Sc \gg 1$. *J. Fluid Mech.* **317**, 21–71.

BUCH, K.A. & DAHM, W.J.A. 1998 Experimental study of the fine-scale structure of conserved scalar mixing in turbulent shear flows. Part 2. $Sc \approx 1$. *J. Fluid Mech.* **364**, 1–29.

DIMOTAKIS, P.E. 2000 The mixing transition in turbulent flows. *J. Fluid Mech.* **409**, 69–98.

FOSS, J., KLEWICKI, J. & DISIMILE, P. 1986 Transverse vorticity measurements using an array of four hot-wire probes. *Tech. Rep.* Michigan State University.

FREYTAG, C. 1978 Statistical properties of energy dissipation. *Boundary-Layer Meteorol.* **14** (2), 183–198.

FRISH, M.B. & WEBB, W.W. 1981 Direct measurement of vorticity by optical probe. *J. Fluid Mech.* **107**, 173–200.

GANAPATHISUBRAMANI, B., LONGMIRE, E.K., MARUSIC, I. & POTHOS, S. 2005 Dual-plane PIV technique to determine the complete velocity gradient tensor in a turbulent boundary layer. *Exp. Fluids* **39** (2), 222–231.

GOHIL, T.B., SAHA, A.K. & MURALIDHAR, K. 2014 Large eddy simulation of a free circular jet. *J. Fluids Engng* **136**, 051205.

HE, L. & LU, X.-G. 2020 Visualization of the shock wave/boundary layer interaction using polarization imaging. *J. Vis.* **23** (5), 839–850.

HEMMILÄ, I. 1993 Progress in delayed fluorescence immunoassay. In *Fluorescence Spectroscopy: New Methods and Applications* (ed. O.S. Wolfbeis), pp. 259–266. Springer.

HU, H., SAGA, T., KOBAYASHI, T., TANIGUCHI, N. & YASUKI, M. 2001 Dual-plane stereoscopic particle image velocimetry: system set-up and its application on a lobed jet mixing flow. *Exp. Fluids* **31** (3), 277–293.

HUSSEIN, H.J., CAPP, S.P. & GEORGE, W.K. 1994 Velocity measurements in a high-Reynolds-number, momentum-conserving, axisymmetric, turbulent jet. *J. Fluid Mech.* **258**, 31–75.

KÄHLER, C.J. 2004 Investigation of the spatio-temporal flow structure in the buffer region of a turbulent boundary layer by means of multiplane stereo PIV. *Exp. Fluids* **36** (1), 114–130.

KASTRINAKIS, E.G. & ECKELMANN, H. 1983 Measurement of streamwise vorticity fluctuations in a turbulent channel flow. *J. Fluid Mech.* **137**, 165–186.

KENYON, A.J., MCCAFFERY, A.J. & QUINTELLA, C.M. 1991*a* Fluorescence depolarization as a probe of molecular dynamics within liquid jets. *Mol. Phys.* **72** (4), 965–970.

KENYON, A.J., MCCAFFERY, A.J., QUINTELLA, C.M. & WINKEL, J.F. 1991*b* A study of molecular dynamics within liquid flows using fluorescence depolarization. *Mol. Phys.* **74** (4), 871–884.

KLEWICKI, J.C. & FALCO, R.E. 1990 On accurately measuring statistics associated with small-scale structure in turbulent boundary layers using hot-wire probes. *J. Fluid Mech.* **219**, 119–142.

LAKOWICZ, J.R. 2006*a* Fluorescence anisotropy. In *Principles of Fluorescence Spectroscopy*, pp. 353–382. Springer.

LAKOWICZ, J.R. 2006*b* Fluorophores. In *Principles of Fluorescence Spectroscopy* (ed. J.R. Lakowicz), pp. 63–95. Springer.

LANG, D.B. & DIMOTAKIS, P.E. 1984 Vorticity measurements in a two-dimensional shear-layer. *Bull. Am. Phys. Soc.* **29**, 1556.

LANG, D.B. & DIMOTAKIS, P.E. 1986 Laser doppler velocity & vorticity measurements in turbulent shear layers. California Institute of Technology. Available at: https://resolver.caltech.edu/CaltechAUTHORS:20141113-163459681.

LI, M. & SELVIN, P.R. 1995 Luminescent polyaminocarboxylate chelates of terbium and europium: the effect of chelate structure. *J. Am. Chem. Soc.* **117** (31), 8132–8138.

LOURENCO, L. & KROTHAPALLI, A. 1986 The role of photographic parameters in laser Speckle of particle image displacement velocimetry. *Exp. Fluids* **5** (1), 29–32.

MEINHART, C. & ADRIAN, R. 1995 Measurement of the zero-pressure gradient turbulent boundary layer using particle image velocimetry. *AIAA Paper* 1995-789.

MUSHRUSH, G.W., STALICK, W.M., WATKINS, J.M. & DEANHARDT, M.L. 1986 Terbium(III) and europium(III) ions as sensitive probes in organic photochemistry. *J. Less Common Metals* **126**, 363–369.

OLSSON, M. & FUCHS, L. 1996 Large eddy simulation of the proximal region of a spatially developing circular jet. *Phys. Fluids* **8** (8), 2125–2137.

PARK, S.J., SHAKYA, A. & KING, J.T. 2019 Depletion layer dynamics of polyelectrolyte solutions under Poiseuille flow. *Proc. Natl Acad. Sci*. **116** (33), 16256–16261.

RICHARDSON, F.S. 1982 Terbium(III) and europium(III) ions as luminescent probes and stains for biomolecular systems. *Chem. Rev*. **82** (5), 541–552.

RYABTSEV, A., POUYA, S., KOOCHESFAHANI, M. & DANTUS, M. 2015 Characterization of vorticity in fluids by a spatially shaped laser beam. In *Laser Resonators, Microresonators, and Beam Control XVII*, vol. 9343, 93431G. International Society for Optics and Photonics.

RYABTSEV, A., POUYA, S., SAFARIPOUR, A., KOOCHESFAHANI, M. & DANTUS, M. 2016 Fluid flow vorticity measurement using laser beams with orbital angular momentum. *Opt. Express* **24** (11), 11762–11767.

SABBATINI, N., GUARDIGLI, M. & LEHN, J.-M. 1993 Luminescent lanthanide complexes as photochemical supramolecular devices. *Coordination Chem. Rev*. **123** (1), 201–228.

SCHMIDT, M.J. 2021 Measurement of flow-induced nanoparticle rotation with luminescence anisotropy. Doctoral Thesis, ETH Zurich.

SCHMIDT, M.J. & RÖSGEN, T. 2021*a* Luminescence Anisotropy of a Round Jet at *Re*12 000 and 14 400. Available at: https://doi.org/10.5281/zenodo.4039456.

SCHMIDT, M.J. & RÖSGEN, T. 2021*b* pyoptivorticity: Toolbox for Luminescence Anisotropy Measurements of Vorticity. Available at: https://doi.org/10.5281/zenodo.4039555.

SCHMIDT, M.J. & RÖSGEN, T. 2021*c* Xanthene-stained nanoparticles for phosphorescence anisotropy measurements. *Exp. Results* **2**, e20.

SCHMIDT, M.J. & RÖSGEN, T. 2023 Influence of deterministic rotations on luminescence anisotropy. *Phys. Rev. Res*. **5** (3), 033006.

SCHNEIDERS, J.F.G., SCARANO, F. & ELSINGA, G.E. 2017 Resolving vorticity and dissipation in a turbulent boundary layer by tomographic PTV and VIC+. *Exp. Fluids* **58** (4), 27.

SIEGEL, J., SUHLING, K., LÉVÊQUE-FORT, S., WEBB, S.E.D., DAVIS, D.M., PHILLIPS, D., SABHARWAL, Y. & FRENCH, P.M.W. 2003 Wide-field time-resolved fluorescence anisotropy imaging (TR-FAIM): imaging the rotational mobility of a fluorophore. *Rev. Sci. Instrum*. **74** (1), 182–192.

STRÖHL, F., WONG, H.H.W., HOLT, C.E. & KAMINSKI, C.F. 2018 Total internal reflection fluorescence anisotropy imaging microscopy: setup, calibration, and data processing for protein polymerization measurements in living cells. *Meth. Appl. Fluoresc*. **6** (1), 014004.

VUKOSLAVĈEVIĆ, P. & WALLACE, J.M. 1996 A 12-sensor hot-wire probe to measure the velocity and vorticity vectors in turbulent flow. *Meas. Sci. Technol*. **7** (10), 1451–1461.

VUKOSLAVĈEVIĆ, P., WALLACE, J.M. & BALINT, J.-L. 1991 The velocity and vorticity vector fields of a turbulent boundary layer. Part 1. Simultaneous measurement by hot-wire anemometry. *J. Fluid Mech*. **228**, 25–51.

WALLACE, J.M. 2009 Twenty years of experimental and direct numerical simulation access to the velocity gradient tensor: what have we learned about turbulence? *Phys. Fluids* **21** (2), 021301.

WALLACE, J.M. & FOSS, J.F. 1995 The measurement of vorticity in turbulent flows. *Annu. Rev. Fluid Mech*. **27** (1), 469–514.

WU, H., XU, H. & BODENSCHATZ, E. 2019 Measuring vorticity vector from the spinning of micro-sized mirror-encapsulated spherical particles in the flow. *Rev. Sci. Instrum*. **90** (11), 115111.

ZIMMERMAN, S., MORRILL-WINTER, C. & KLEWICKI, J. 2017 Design and implementation of a hot-wire probe for simultaneous velocity and vorticity vector measurements in boundary layers. *Exp. Fluids* **58** (10), 148.

ZIMMERMAN, S., *et al.*2019 A comparative study of the velocity and vorticity structure in pipes and boundary layers at friction Reynolds numbers up to 10^4. *J. Fluid Mech*. **869**, 182–213.